Perforation of welded aluminum components: microstructure-based modeling and experimental validation

Jens Kristian Holmen[a,*], Tore Børvik[a,b], Ole Runar Myhr[c], Hallvard Gustav Fjær[d], Odd Sture Hopperstad[a]

[a] *Structural Impact Laboratory (SIMLab), Centre for Research-based Innovation (CRI), Department of Structural Engineering, Norwegian University of Science and Technology, NO-7491 Trondheim, Norway*
[b] *Norwegian Defence Estates Agency, Research and Development Section, NO-0103 Oslo, Norway*
[c] *Hydro Aluminium, Research and Technology Development (RTD), NO-6601 Sunndalsøra, Norway*
[d] *Institute for Energy Technology, NO-2027 Kjeller, Norway*

Abstract

Perforation of welded aluminum structures by small-arms bullets is studied both experimentally and numerically in this paper. From the chemical composition, artificial aging history, and welding procedure, the spatial distribution of the flow stress at ambient temperature of MIG-welded AA6082-T6 aluminum extrusions was determined by using a thermal finite element model and a nano-scale material model. The resulting flow-stress curves which are functions of the distance from the weld center line were used in a mechanical 3D finite element model to investigate the effect of the heat affected zone (HAZ) on the ballistic properties of welded aluminum extrusions. For experimental validation, 10 mm, 20 mm and 30 mm thick extruded profiles were processed and welded to correspond to the numerical method. Hardness measurements and ballistic impact experiments were performed in the weld metal, HAZ, and base material. Uniaxial tension tests were conducted for the base material of the 10 mm and 30 mm profiles. These tests provided sufficient data for experimental validation of the numerical method. Temperature distribution, hardness values, equivalent stress-strain curves, and ballistic limit curves are reported from both the experiments and the numerical simulations. In general, the experimental results correspond well with the numerical predictions and the predicted ballistic limit velocities are conservative, suggesting that this method is a possible alternative to performing expensive and time consuming experimental testing in the early stages of the design of protective aluminum structures. The HAZ is found to impair the ballistic performance locally, but the difference between the ballistic limit for the base material and HAZ was never more than 10% in this study.

*Corresponding author. Tel.: +47 93 04 58 37
Email address: jens.k.holmen@ntnu.no (Jens Kristian Holmen)
URL: www.ntnu.edu/simlab (Jens Kristian Holmen)

Keywords: Ballistics, Impact, Aluminum alloy, MIG welding, Numerical methods

1. Introduction

Most studies concerning the ballistic capabilities of structures involve perpendicular impact on flat, flawless surfaces where the effects of connections are disregarded [1–5]. However, size and shape limitations inherent in ordinary construction processes make the presence of e.g. welds, nuts, or bolts inevitable. Consequently, knowledge about connections is essential in any design situation. In the design of protective structures against small-arms bullets, thin plates made of steel are widely used due to their advantageous combination of strength, hardness, ductility, and relatively low price compared to most other armor materials [6]. However, when areal mass is taken into account, high-strength aluminum alloys can rival the ballistic properties of high-strength steels [7, 8].

Welding is a common and effective joining procedure, but welding of aluminum generates a zone which may be weak relative to the base material. This zone is known as the heat affected zone (HAZ), and it may cause a so-called ballistic window in protective structures. Usually material strength governs ballistic performance [6, 9], so special attention is required in the design of welded aluminum protective structures.

The strength and work hardening of Al-Mg-Si aluminum alloys can be predicted with reasonable accuracy by nano-scale material models [10–13]. The application of such a model was shown by Johnsen et al. [14], where the stress-strain behavior of four different heat treatments (tempers) of the wrought aluminum alloy AA6070 were determined with a nanostructure model, NaMo. The model was able to predict the yield strength and work hardening of the different tempers. Subsequently, mechanical non-linear finite element simulations, using the yield strength and work-hardening determined with NaMo as input, accurately described the ballistic behavior. This correlation indicates that employing the predictive capabilities of nano-scale material modeling in combination with tools that can provide thermal histories in all material points due to welding can dramatically reduce the need for expensive and time-consuming experimental programs.

Computational models which were designed to incorporate elements of the manufacturing process for conventionally or friction-stir welded steel and aluminum protective structures have also been of interest for several years [15–17]. These techniques are often called through-process modeling. In some cases, the

ballistic behavior is included in the model [18–21].

There are two main objectives of this paper. First, we investigate how welding affects the ballistic properties of aluminum extrusions of various thicknesses through an extensive experimental program for 10 mm, 20 mm and 30 mm thick profiles, including tension tests for the 10 mm and 30 mm profiles; hardness measurements of the base material, HAZ, and weld for all thicknesses; and ballistic impact experiments. In the ballistic tests, armor piercing (AP) bullets are fired at the welded test specimens at various distances from the weld center line. Second, and most important in this study, a purely numerical method is demonstrated. The numerical approach is performed independently from the experiments. Hence, the experimental results are only used for validation purposes in this part of the paper. The heat distribution from multi-pass welding is calculated numerically by the thermal finite element program WELDSIM [22]. Results from selected points in these analyses are used as inputs to NaMo [23] to determine the yield strength and hardening behavior of the material as functions of distance from the weld center line, before the non-linear finite element code IMPETUS Afea Solver [24] is employed to solve the impact problem itself. All the calculations can be done without carrying out a single experiment.

Sections 2 and 3 present an experimental program in which the material processing, welding procedure, material testing, and ballistic testing are carried out to obtain an experimental basis for comparison with, and validation of, the subsequent numerical results. Section 4 outlines the numerical scheme and provides a description of the use of WELDSIM, NaMo and IMPETUS Afea Solver. In Section 5 the numerical predictions are presented, discussed, and compared to the experimental results. The main observations and conclusions are summarized in Section 6.

2. Material

2.1. Material processing and welding

Extruded 10 mm, 20 mm and 30 mm thick profiles made of AA6082-T6 were investigated in this study. The measured chemical compositions of the extrusions provided by Hydro Aluminium and the composition window of AA6082 are shown in Table 1. Due to the varying profile thicknesses, the artificial aging to obtain the peak strength temper T6 varied. The 10 mm extrusion was held at 175° for 5 h and 30 min, while the 20 mm and 30 mm thick extrusions were held at 185° for 5 h and 10 min.

The flat extruded profiles were automatically welded to each other with MIG welding at Marin Aluminium AS. Precautions were taken to ensure that the welding process was in accordance with EN 1090-3

Table 1: Chemical composition of the various profiles, and composition window for AA6082 in wt-%

	Si	Mg	Mn	Fe	Ti	Zn	Cu	Cr	Al
Measured - 10 mm profile	0.93	0.60	0.55	0.18	0.011	0.002	0.008	0.011	Balance
Measured - 20 mm profile	0.99	0.63	0.56	0.17	0.018	0.006	0.025	0.011	Balance
Measured - 30 mm profile	0.97	0.63	0.54	0.16	0.013	0.004	0.004	0.013	Balance
Composition window AA6082	0.7-1.3	0.6-1.2	0.4-1.0	0.50	0.10	0.20	0.10	0.25	Balance

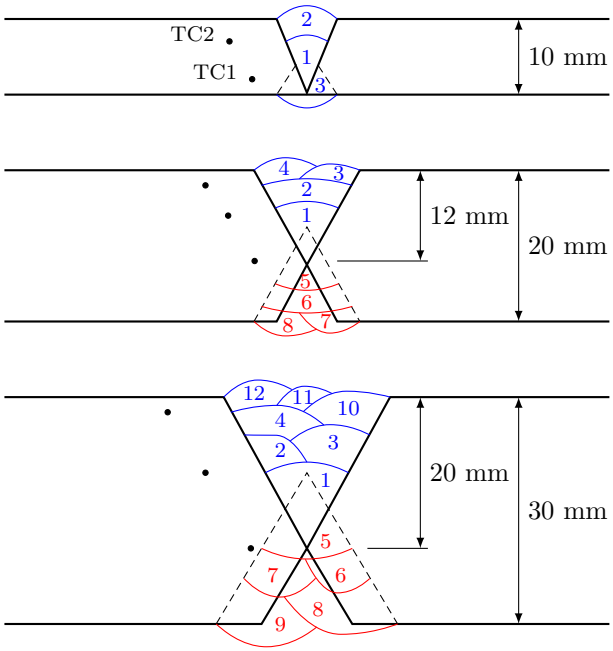

Figure 1: Numbering of weld-seams in the multipass welding procedure. Placements of the thermocouples are indicated with dots.

[25]. Numbering of the various weld seams in the multi-pass welding procedures is shown in Fig. 1. In all welding procedures the temperature of the HAZ was measured to be below 100 °C before the next weld seam was initiated. The welding consumable was a Safra 5183 welding wire designed for high corrosion environments such as ship constructions and offshore applications ($\sigma_{0.2}$ ≥125 MPa [26]). Complex thermal histories were introduced during welding due to the application of three weld passes for the 10 mm profile, eight for the 20 mm profile, and twelve for the 30 mm profile. The temperature-time histories were measured by thermocouples. The placement of these thermocouples is shown in Fig. 1, while selected results from the temperature measurements are shown later in the paper.

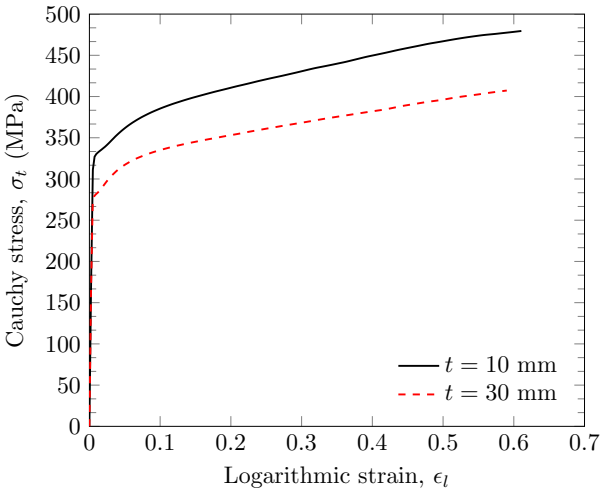

Figure 2: Typical Cauchy stress-logarithmic strain curves from experimental tension tests taken from a 10 mm thick profile and a 30 mm thick profile.

2.2. *Material testing*

Three tensile tests of the base material were performed in both the extrusion direction (0°) and the cross-weld direction (90°) for the 10 mm and 30 mm thick extruded profiles. Two typical curves from the 0°-direction are shown in Fig. 2. A Zwick Roell 30 kN tensile testing machine was used with a cross-head velocity of 1.2 mm/min. This corresponds to an initial strain rate of 5×10^{-4} s^{-1} for the circular test specimens with an initial gauge-length of 70 mm and an initial diameter, $d_0 = 6$ mm (see e.g. Holmen et al. [9] for the specimen geometry). Diameter reduction was continuously measured in two perpendicular directions all the way to fracture by a laser-scan micrometer [27]. Assuming plastic incompressibility the Cauchy stress σ_t and logarithmic strain ϵ_l are calculated from the measured force, F, and the diameters in the thickness direction of the extrusion (d_z) and transverse direction of the specimen ($d_\perp$) as

$$A = \frac{\pi}{4} d_z d_\perp, \qquad \sigma_t = \frac{F}{A} \qquad \text{and} \qquad \epsilon_l = \ln\left(\frac{A_0}{A}\right) \tag{1}$$

where A_0 is the initial area of the specimen. There is no significant difference in yield strength, flow stress or failure strain obtained from the tests in the 0° and 90°-directions for the 10 mm thick profile. Some anisotropy was seen for the yield strength of the 30 mm thick profile (the 90°-direction is approximately 25 MPa weaker than the 0°-direction). The scatter between repeated tests was less than 1% in yield stress and less than 4% in failure strain.

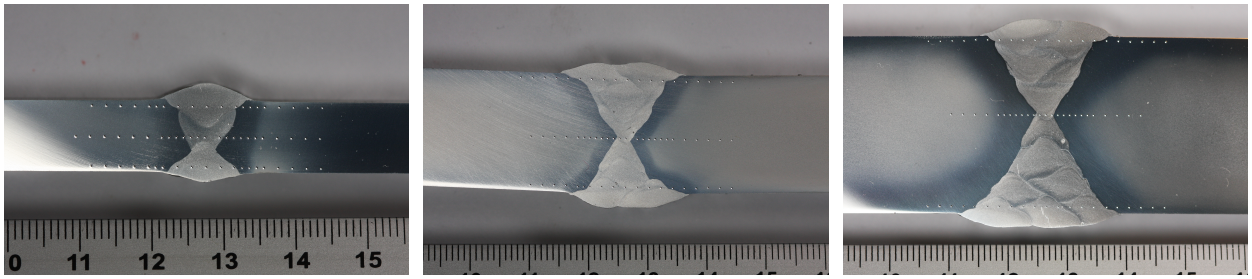

(a) 10 mm (b) 20 mm (c) 30 mm

Figure 3: Pictures of the cross section of the welds. The dots are indentations made by the hardness test machine.

To pinpoint the location of the HAZ and to reveal the strength differences caused by the temperature history, hardness testing was conducted. The specimens are shown in Fig. 3, and they were tested with 5 kg of pressure for 15 seconds each in a Struers DuraScan fully automatic Vickers hardness testing machine. Hardness measurements were conducted along three horizontal lines across the weld, as well as along one vertical line in the thickness direction of the base material. Plots of the Vickers hardness can be seen in Fig. 4. An investigation of these curves shows that the 10 mm and 20 mm profiles exhibit practically equal hardness distributions, while the 30 mm profile is markedly weaker. Further investigation of Fig. 4 reveals that the lowest hardness values for each through-thickness position of the cross section follow a line offset from the fusion line, approximately 6 mm for the 20 mm thick profile (Fig. 4d) and 7 mm for the 30 mm thick profile (Fig. 4f). For the 10 mm thick profile the lowest hardness values are located along a nearly straight vertical line (Fig. 4b). The average hardness and the sample standard deviation (s) in the base material for the 10 mm, 20 mm and 30 mm thick extruded profiles are 110 HV (s = 0.4 HV), 105 HV (s = 1.3 HV) and 89 HV (s = 1.2 HV), respectively, showing that the hardness (and strength) decreases as the extrusion thickness increases. However, based on these measurements the material behavior of the 10 mm and 20 mm extrusions is assumed to be equal.

The reason for the observed lower base-metal hardness of the 30 mm thick extrusion compared with the two other thicknesses is a lower cooling rate following the extrusion process for this relatively thick profile. 6082-type alloys are known to be quench sensitive, and since the cooling rate decreases with increasing thickness, it has probably been sufficiently slow to cause severe precipitation of coarse non-hardening particles during the cooling stage as described in Myhr et al. [28].

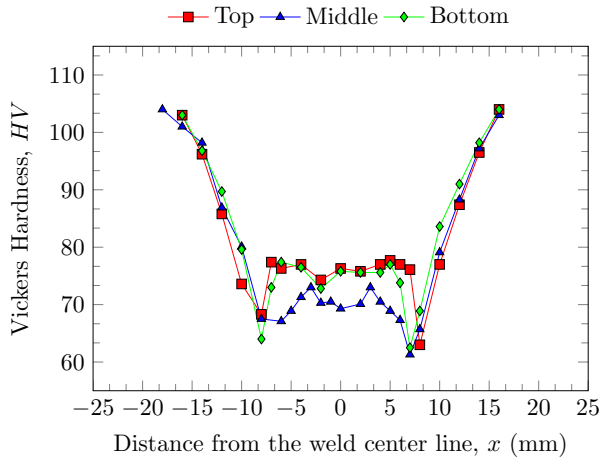

(a) t = 10 mm

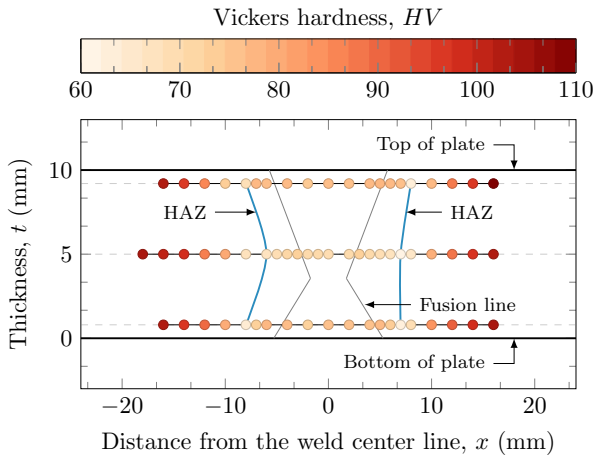

(b) t = 10 mm

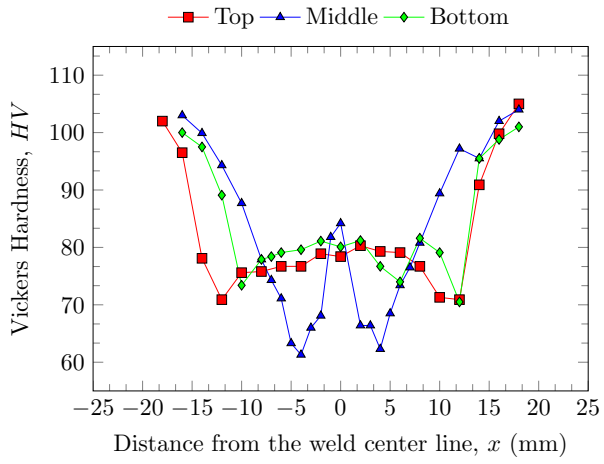

(c) t = 20 mm

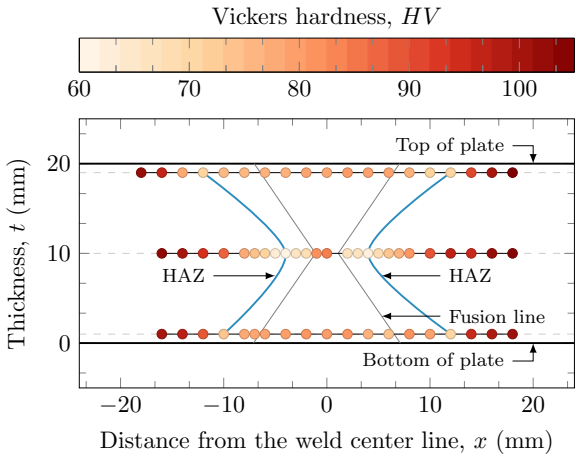

(d) t = 20 mm

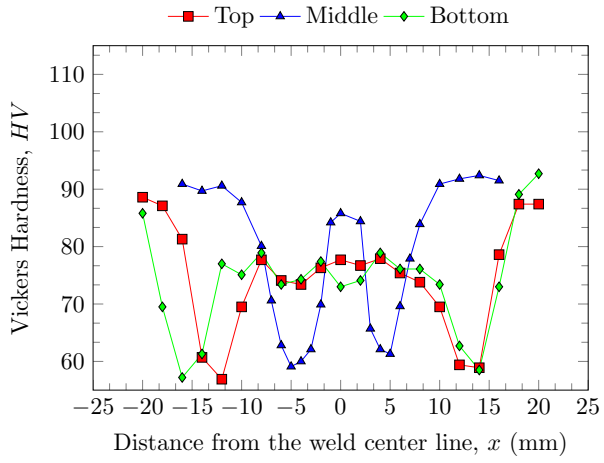

(e) t = 30 mm

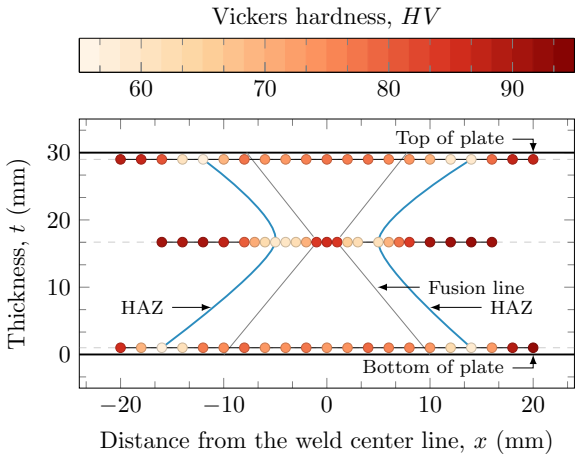

(f) t = 30 mm

Figure 4: Overview of the hardness measurements: (a), (c) and (e) show the Vickers hardness value as the ordinate for the three test strings for each profile; (b), (d) and (f) show the Vickers hardness value for each indentation represented by a color. The lowest HV measurements in the HAZ and the fusion lines are indicated [29].

3. Ballistic experiments

The ballistic impact experiments were performed in the ballistic laboratory at SIMLab, NTNU. The 7.62 mm AP-bullets shown in Fig. 5 were fired from a smooth-bore Mauser rifle inside a 16 m^3 protective tank. The bullet velocity was controlled by adjusting the amount of powder in the cartridge before each shot. Detailed description of the ballistic setup and bullet are provided by Børvik et al. [30, 31]. All shots were fired from a safe distance using a magnetic trigger, and the initial and residual velocities of the bullet were measured optically with a Phantom v1610 high speed camera operating at 75,000 fps. The welds were milled flush to obtain a constant thickness before ballistic testing. Pictures of the perforation process are shown in Fig. 6. In most of the tests the jacket was completely ripped off the core and fragmented into several pieces, but the core itself remained rigid and undamaged (by visual inspection) during impact in all tests. A total of 25 shots were fired at the various parts of the respective profiles, i.e. 8-9 shots for each thickness. One shot hit directly in each weld, whereas three or four shots hit the base material and the HAZ. A shooting-map for the 10 mm thick profile is shown in Fig. 7, and the results are plotted in Fig. 8. Every shot obtained full perforation of the profiles so the ballistic limit velocity, v_{bl}, was estimated by minimizing the mean-squared-error between the solid lines and data points shown in Fig. 8. The solid lines estimate the predicted residual velocity, v_r, based on a model originally proposed by Recht and Ipson [32]

$$v_r = \left(v_i^2 - v_{bl}^2\right)^{1/2}, \tag{2}$$

where v_i and v_{bl} are the initial velocity and ballistic limit velocity, respectively. This simple equation, also known as the Recht and Ipson model for rigid sharp projectiles, has been shown to represent perforation experiments with sharp projectiles on ductile targets accurately [33]. Note that the Recht-Ipson model was originally derived for rigid penetrators, which seems like a reasonable assumption in these tests.

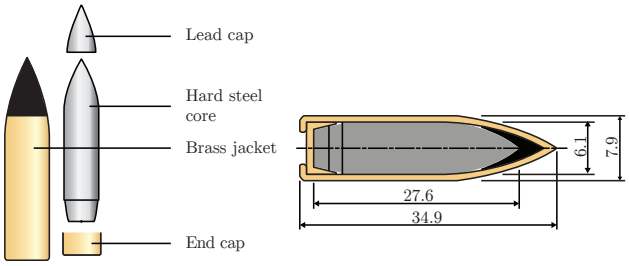

Figure 5: Geometry of the AP-bullet used in the experiments.

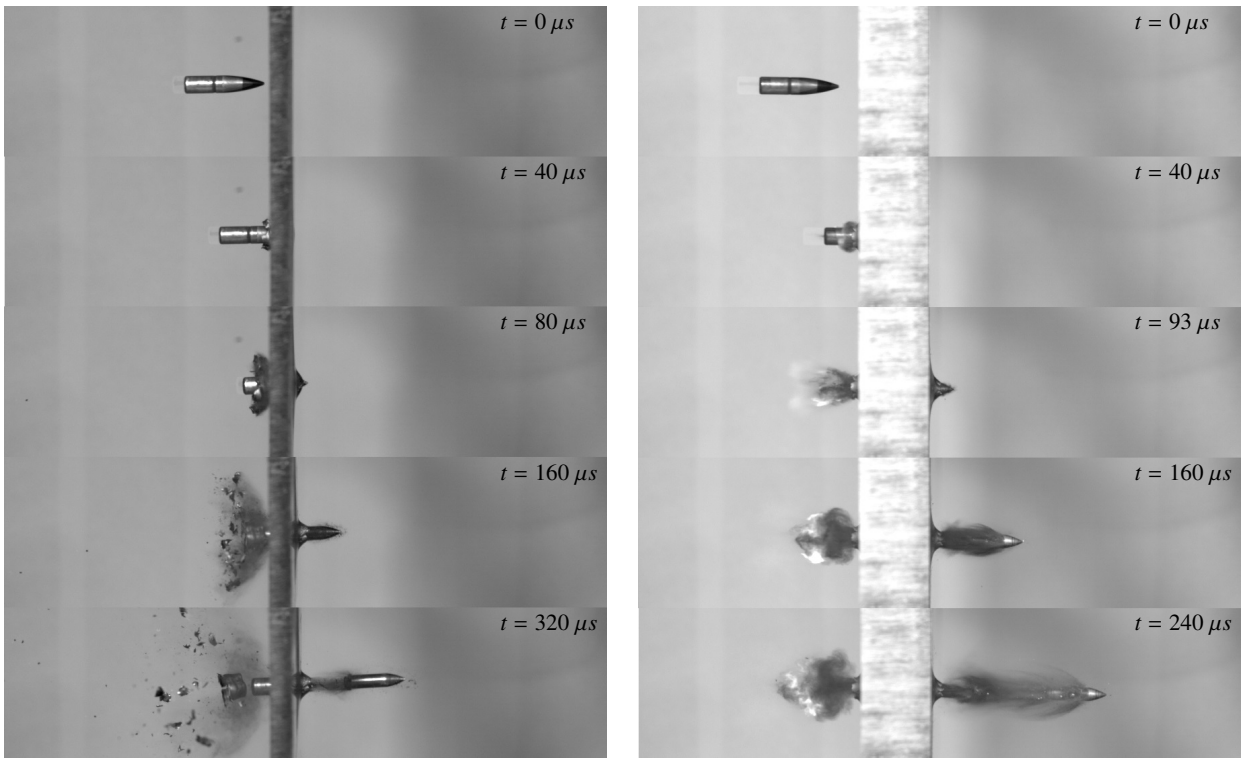

(a) (b)

Figure 6: Sequences of images showing the perforation process of the base material of: (a) a 10 mm thick AA6082-T6 extrusion (v_i = 390.6 m/s, v_r = 179.2 m/s) and (b) a 30 mm thick AA6082-T6 extrusion (v_i = 726.8 m/s, v_r = 457.2 m/s).

It can be seen in Fig. 8 that welding affects the ballistic properties of the aluminum alloy, but the effect is not large. It also seems that there is a rather linear relationship between thickness and ballistic limit velocity. For the 10 mm profile the base material is the strongest, and impacts in the weld and HAZ give 3% and 10% lower ballistic limit velocities respectively. Impacts on the 20 mm profile show the same trend, i.e. the base material is the strongest. In this profile, however, the weld and HAZ exhibit equal resistance against perforation and their ballistic limit velocities are both 6% lower than for the base material. Looking at the 30 mm thick profile we see that the weld is actually slightly stronger than the base material with a 1% increase in the ballistic limit velocity. Also here the HAZ is the weakest with a 3% lower ballistic limit velocity than the base material. A clear correlation can be seen between the hardness measurements in Fig. 4 and the ballistic curves in Fig. 8. The hardness of the weld metal is significantly lower than that of the base material for the 10 mm and 20 mm thick profiles, whereas for the 30 mm profile the weld metal hardness is almost at the same level as the base material. The HAZ is the weakest zone in every case.

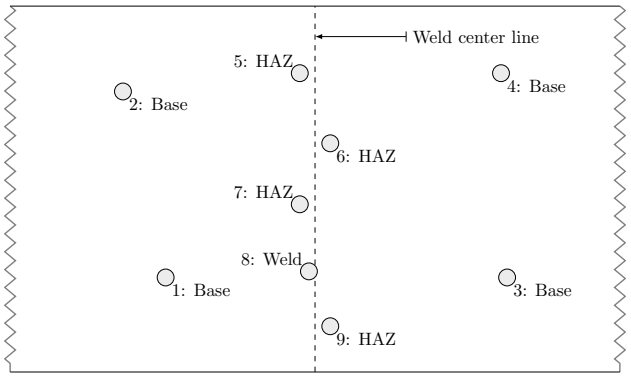

Figure 7: Shooting map.

Examples of some typical post-perforation bullet-holes are shown in Fig. 9. As these pictures indicate, the predominant failure mode in all the experiments was ductile hole-growth which was sometimes accompanied by moderate rear-face petaling without fragmentation.

It should be noted that these results are based on a limited set of data, in particular for impact in the welds with only one hit for each profile. It was hard to directly hit the weld, and due to limited amount of material available for testing the shots were fired in close proximity to each other. However, at least one projectile diameter (but normally 3-4) was left between each point of impact. Based on the results presented in Fig. 8, this did not seem to have any noticeable effect on the ballistic data.

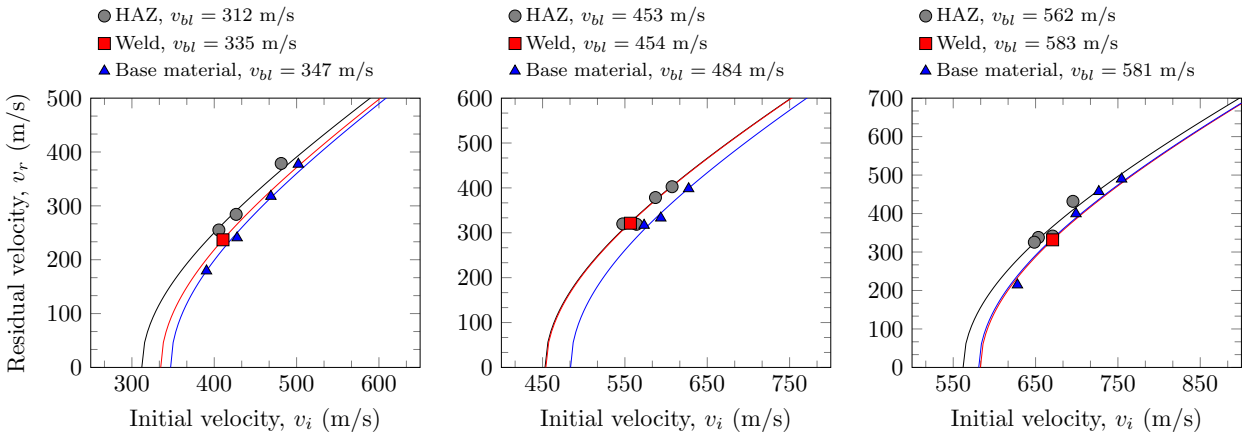

(a) t = 10 mm (b) t = 20 mm (c) t = 30 mm

Figure 8: Ballistic curves obtained experimentally from (a) the 10 mm thick profile, (b) the 20 mm thick profile, and (c) the 30 mm thick profile.

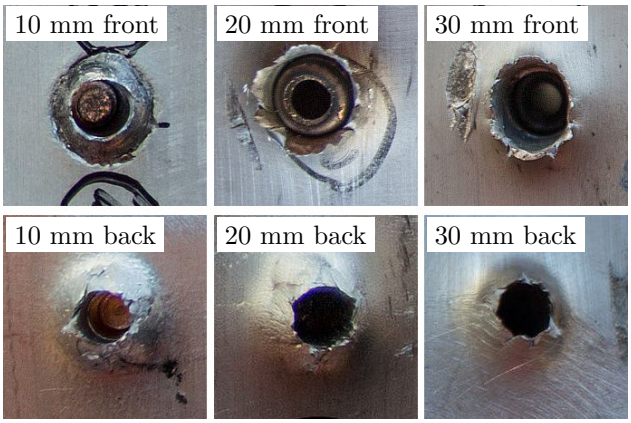

Figure 9: Some typical bullet holes from impacts on the base material.

4. Numerical methods

4.1. Outline

The three-step numerical procedure employed in this paper is illustrated in Fig. 10. First a thermal solver (WELDSIM) is used to predict the thermal field from the welding. Then a nano-scale material model (NaMo) makes use of the chemical composition and the complete temperature history from aging and welding as input in order to calculate the flow-stress curves which are used by a mechanical finite element solver (IMPETUS Afea Solver) to simulate the ballistic experiments. No experimental data whatsoever has been used for calibration of the numerical models in this section. The numerical calculations are limited to the 10 mm thick extrusion since the procedure will essentially be identical for thicker profiles.

4.2. WELDSIM

The evolution of the temperature field during the welding was simulated with the thermal solver WELDSIM [22, 23, 34]. WELDSIM can be used to predict the evolution of temperatures, microstructure parameters and stresses during the welding process. However, in this analysis only the thermal module was applied. Symmetry along the weld center line was assumed and a 0.8 m section of the actual extrusion length of 2 m was included in the solution domain. By applying a typical arc efficiency for MIG-welding of 0.8 (i.e., the net power fraction received by the weldment when taking into account losses due to convection and radiation) and the recorded values of current, voltage and welding speed, the simulated temperature-time histories were very close to the measured temperature-time histories, as shown in Fig. 11.

The handling of multipass welding has previously been applied for simulation of steel welding [35, 36]. The weld metal domains are predefined by the preprocessing. Elements in domains corresponding to weld

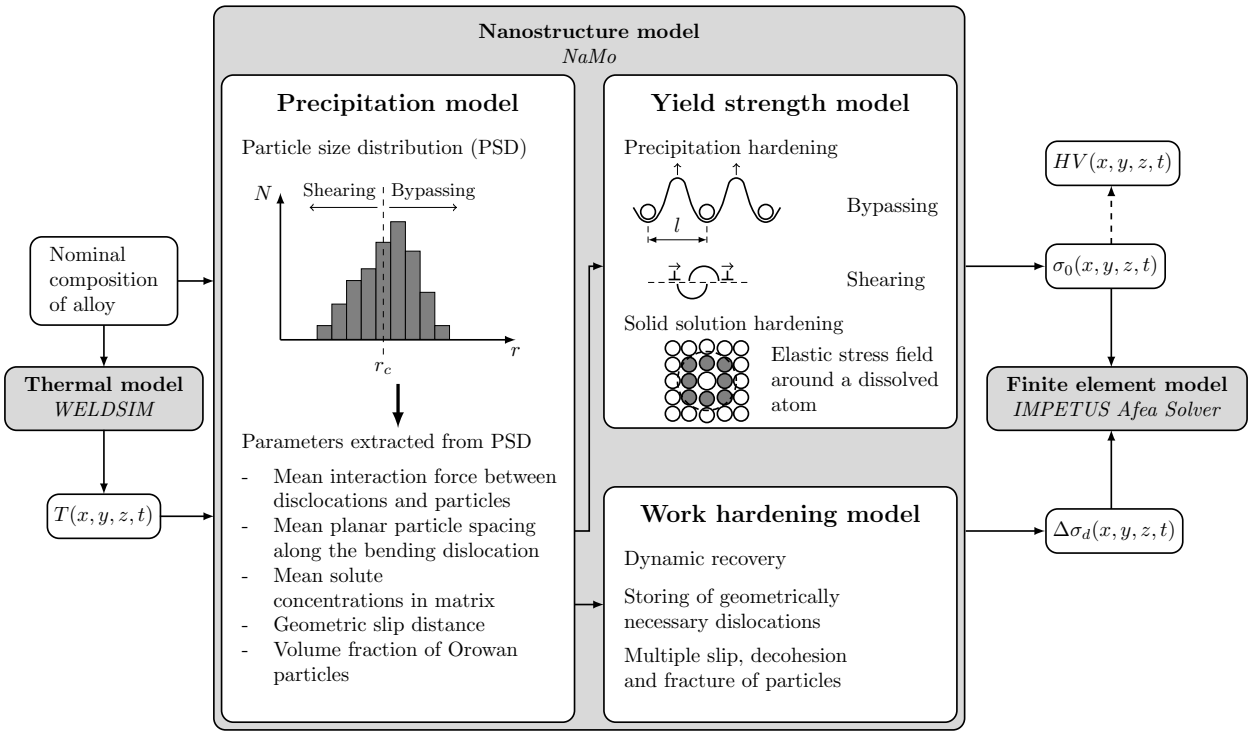

Figure 10: Overview of the relative dependencies of the numerical models applied in this current study.

metal becoming deposited in later passes are not activated during the first pass. The weld groove for the third pass was in this case made after welding of the first two passes. This was accounted for in the simulation by redefining this domain to become a filler metal domain in a restart simulation of the third weld pass. A temperature field from this pass is depicted in Fig. 12 together with the finite element mesh illustrating the activation of elements in the weld.

In Fig. 13 the peak temperatures in a central cross-section and at the top surface of the solution domain are shown. The leftmost contour line corresponds to the computed fusion line. This appears to be in good agreement with the picture shown in Fig. 3a.

4.3. Microstructural changes during welding and natural aging

The microstructure changes taking place during welding and room temperature storing are explained in Fig. 14, which is based on Myhr et al. [28, 37]. During artificial aging, a high density of fine, needle-shaped β'' particles form uniformly in the matrix, which is the dominating hardening phase in T6 heat-treated Al-Mg-Si alloys. However, since these precipitates are thermodynamically unstable in a welding situation, the smallest ones start to dissolve in parts of the HAZ where the peak temperature has been above approximately

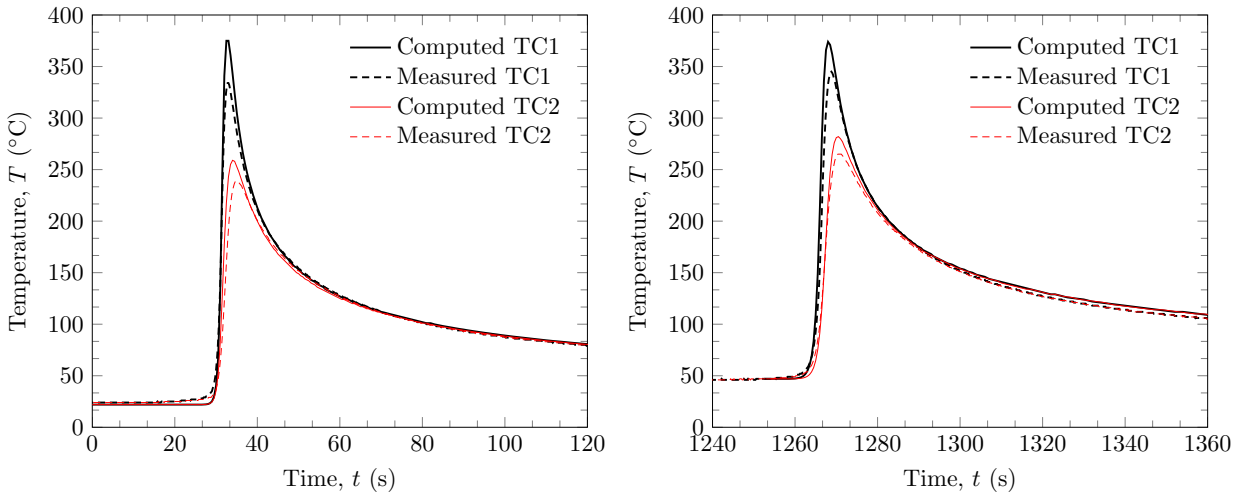

Figure 11: Comparison of computed temperatures and temperatures measured by thermocouples (TC), (a) during the first weld pass, and (b) during the second weld pass.

250°C, while the larger ones continue to grow. Close to the weld fusion line, i.e. Zone 1 in Fig. 14, full reversion of the β'' particles is achieved. At the same time, coarse rod-shaped β' precipitates may form in the intermediate peak temperature range between 250°C and 480°C, as indicated in Zone 2 in the figure. These β' precipitates will grow rapidly in the presence of the abundant solute being supplied from the small, dissolving β'' precipitates.

If welding is succeeded by room temperature storing, natural aging leads to cluster formation in the high peak temperature regions of the HAZ corresponding to Zone 1 in Fig. 14. It occurs depending both on the matrix vacancy concentration and the level of Mg and Si in solid solution. Accordingly, the cluster

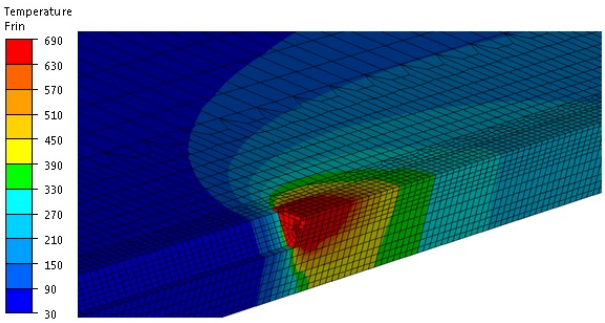

Figure 12: The temperature field in °C during the third weldpass.

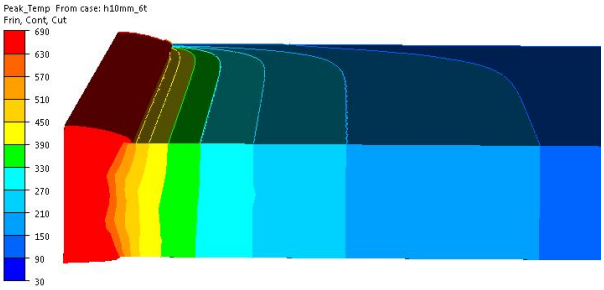

Figure 13: Peak temperatures in °C shown on a central cross-section and the top surface of the solution domain.

formation would be expected to be most extensive in the fully reverted region close to the weld fusion line owing to the combined effect of a high solute content and a high concentration of quenched-in vacancies. Conversely, the cluster formation will be suppressed in parts of the HAZ where the peak temperature is lower because the aluminum matrix in these regions will be depleted with respect to vacancies and solute. This eventually leads to the development of a permanent soft region within the HAZ after prolonged room temperature storing in agreement with experimental observations.

4.4. Nanostructure Model (NaMo)

Fig. 10 describes the components of the nano-scale material model NaMo which is a combined precipitation, yield strength and work hardening model for age-hardening aluminum alloys [12, 13]. The present version is comprehensively verified and validated for 6xxx series aluminum alloys (see e.g. Myhr et al. [11, 12], Myhr and Grong [13], Johnsen et al. [14], Myhr et al. [28, 37], Dørum et al. [38]). The three submodels shown in Fig. 10 are fully integrated in a computer code, where the outputs from the precipitation model are inputs to both the yield-strength model and the work-hardening model that assumes isotropic material behavior.

In order to run a simulation, the alloy composition and the temperature-time history must be specified. In the current study the temperature-time history is obtained from WELDSIM. Based on the acquired information the complete room-temperature flow-stress curve is calculated by the program. The first step of a simulation is to invoke the precipitation model that calculates the evolution of the hardening precipitates by nucleation, growth or dissolution, and coarsening [11, 12, 28]. Fig. 10 shows a discrete particle size distribution (PSD), where each column corresponds to a certain number density of particles within the specific size class. The PSD changes continuously during heat treatment and welding as calculated by the precipitation model. Based on the PSD, the essential precipitation parameters can be extracted and transferred to

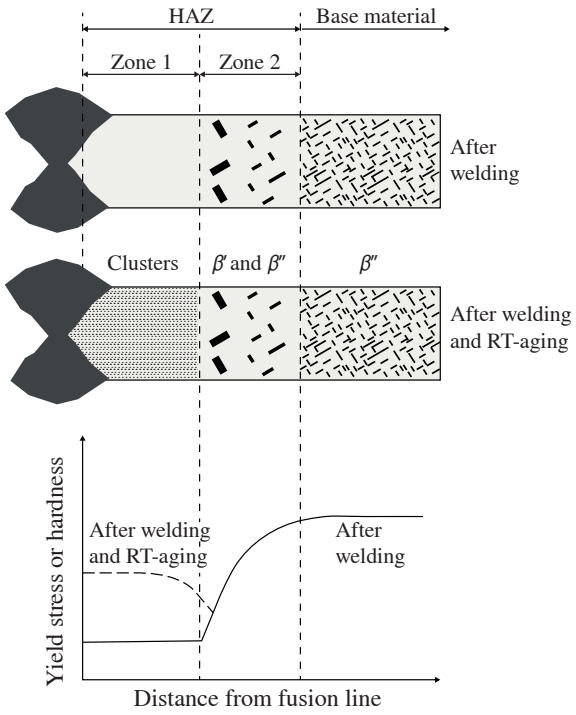

Figure 14: Microstructural changes during welding and natural aging.

the yield-strength and work-hardening models as illustrated in Fig. 10.

In the yield-strength model, the overall macroscopic yield stress σ_0 is given as

$$\sigma_0 = \sigma_i + \sigma_p + \sigma_{ss} \tag{3}$$

where σ_i corresponds to the intrinsic yield stress of pure aluminum, σ_p is the overall precipitation hardening contribution, and σ_{ss} is the contribution from alloying elements in the solid solution. The simplified method described in Myhr and Grong [39] is adopted here to predict the effect of cluster formation and an associated yield strength increase during room temperature storing in regions where the peak temperature has been sufficiently high to cause partial or complete dissolution of the hardening β'' particles during the welding, i.e. Zone 1 in Fig. 14. In order to compare the predicted strength in the HAZ against hardness measurements, a conversion from yield strength (in MPa) to hardness HV (in VPN) via a simple regression formula from Myhr et al. [11] is necessary

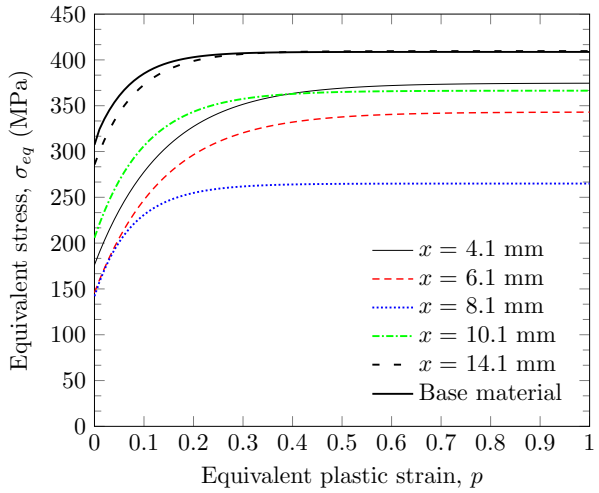

Figure 15: The resulting flow-stress curves obtained from NaMo. These curves determine the hardening behavior in the constitutive model used in IMPETUS Afea Solver. Here x is defined as the distance from the weld center line.

$$HV = 0.33\sigma_0 + 16.0 \tag{4}$$

The work-hardening model predicts the individual evolution of statistically stored and geometrically necessary dislocations, respectively, based on well established evolution laws. The evolution of statistically stored dislocations is predicted as the balance between statistical storage and dynamic recovery of dislocations, while the generation of geometrically necessary dislocations during plastic deformation is assumed to be associated with non-shearable particles. When the two contributions to the overall dislocation density are predicted, the resulting net contribution from dislocation hardening $\Delta\sigma_d$ is calculated from a response equation as a function of the plastic strain, as described in Myhr et al. [12]. Finally, the flow stress σ_f is calculated as follows

$$\sigma_f = \sigma_0 + \Delta\sigma_d \tag{5}$$

Here σ_0 and $\Delta\sigma_d$ are the room temperature yield stress and the net contribution from dislocation hardening, respectively. This allows the complete stress-strain curve to be calculated and transferred to the IMPETUS Afea Solver.

The flow-stress curves for various distances from the weld center line resulting from NaMo simulations are presented in Fig. 15, while Fig. 16 compares the experimental hardness distribution to the values predicted by NaMo for the 10 mm profile using Eq. (4). It is interesting to note that one week of room temperature storage has a pronounced effect on the predicted hardness distribution in the regions close to the weld.

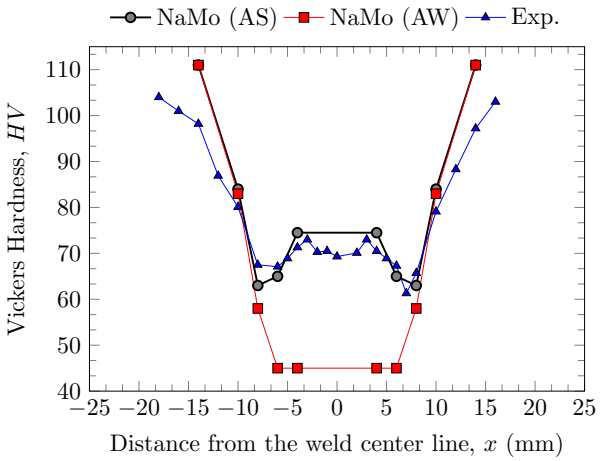

Figure 16: Vickers hardness values obtained from NaMo compared to an experimental curve. NaMo (AS) = hardness values after one week of storage at room temperature while NaMo (AW) = hardness values directly after welding.

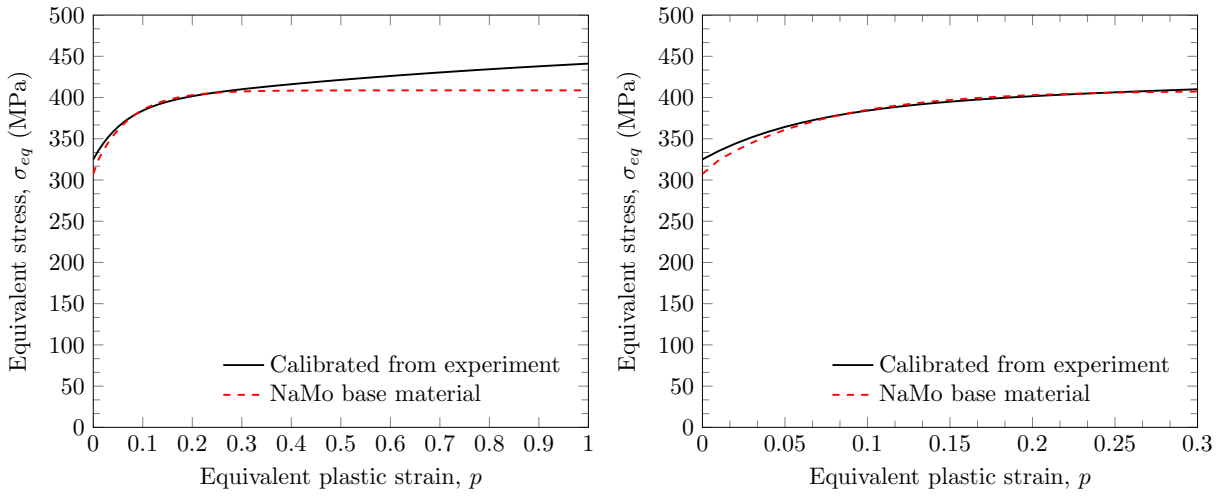

Figure 17: Equivalent stress-equivalent plastic strain curves taken from the numerical work (WELDSIM - NaMo) and a Bridgman-corrected curve from the experiments for (a) $p \in [0; 1]$, and (b) $p \in [0; 0.3]$.

To see how well the numerical method coincides with the experimental results for the base material, the hydrostatic contribution to the true stress-strain curve in Fig. 2 has been removed by use of the Bridgman correction [40] and plotted with the flow-stress curve obtained from NaMo for the base material. The comparison is shown in Fig. 17. The correspondence is seen to be good, especially for plastic strains up to $p = 0.3$ as shown in Fig. 17b.

4.5. IMPETUS Afea Solver

The explicit finite element code IMPETUS Afea Solver [24] was used to simulate the impact process in this paper. A modified Johnson-Cook constitutive relation was chosen to represent the material behavior in the mechanical finite element simulations, i.e. the von Mises yield criterion, the associated flow rule and an isotropic hardening rule are assumed [41]. This can be done because the material was found to be practically isotropic, see Section 2. Thus, the constitutive relation is expressed as

$$\sigma_{eq} = \left(\sigma_0 + \sum_{i=1}^{2} Q_i(1 - \exp(-C_i p))\right)\left(1 + \dot{p}^*\right)^c \left(1 - T^{*m}\right) \tag{6}$$

where σ_{eq} is the equivalent stress, p is the equivalent plastic strain, $\dot{p}^* = \dot{p}/\dot{p}_0$ is the dimensionless plastic strain rate and $T^* = (T - T_r)/(T_m - T_r)$ is the homologous temperature. Here $\dot{p}_0$ is a reference strain rate, T is the absolute temperature, T_r is the ambient temperature and T_m is the melting temperature. Adiabatic heating was assumed in all simulations, and the incremental temperature evolution is calculated using

$$\Delta T = \int_0^p \frac{\chi}{\rho C_p} \sigma_{eq} \mathrm{d}p \tag{7}$$

where χ is the Taylor-Quinney coefficient, C_p is the specific heat, and ρ is the material density. The material strength terms σ_0, Q_1, C_1, Q_2 and C_2 required in the extended Voce hardening rule are summarized in Table 2. They were found by curve-fitting to the equivalent stress-equivalent plastic strain curves obtained by NaMo in Section 4.4. All other model parameters are taken from the literature and given in Table 3. The strain-rate sensitivity of a similar material was investigated by Chen et al. [42] and found to be almost negligible, justifying the low value of c used in the simulations. A linear degradation of strength is introduced in the model through the homologous temperature parameter $m = 1$. This is common in impact analyses, see e.g. Børvik et al. [6].

Table 2: Parameters for the extended Voce hardening rule fitted to the equivalent stress-equivalent plastic strain curves found by NaMo in Fig. 15.

Distance from center weld (mm)	σ_0 (MPa)	Q_1 (MPa)	C_1	Q_2 (MPa)	C_2	Comment
0 mm and 4.1 mm	176.3	198.4	7.2	-	-	At fusion line
6.1 mm	146.0	187.1	7.2	-	-	
8.1 mm	142.1	19.7	23.3	103.2	11.7	Weakest
10.1 mm	205.8	69.5	11.5	91.1	8.7	
14.1 mm	285.6	125.0	12.2	-	-	
Base material	307.3	4.3	278.7	97.1	14.1	Strongest

Table 3: Physical constants and model parameters used in IMPETUS Afea Solver [9].

E (MPa)	ν	ρ (kg/m^3)	m	c	$\dot{p}_0$ s^{-1}	T_r (K)	T_m (K)
70,000	0.3	2700	1	0.001	5×10^{-4}	293	923

By recognizing that high-velocity impact is an extremely localized process, virtually unaffected by the boundary [43], we only need to model a partition of the profile. To save additional computational time, the inherent symmetry of the problem was exploited by modeling only 30° of the target and projectile. A picture of the calculation model and its mesh is shown in Fig. 18. Ten cubic elements, known to be excellent in describing bending, were used over the target thickness, i.e. an element size of 1 mm (Δz = 1 mm). Note that by using the cubic elements the effective node spacing was: Δz = 0.33 mm, giving 61 nodes over the thickness. Sufficient information to calibrate a failure criterion could not be extracted from NaMo, so to allow the projectile to pass through the material a pinhole with a radius of 0.25 mm was introduced in the target's mesh. The pinhole enables us to effectively circumvent the need for a fracture criterion in ballistic perforation using pointed-nose projectiles, and its size was chosen as small as possible without introducing numerical difficulties. In problems where ductile hole growth is expected to be the predominant failure mode the effect of such a pinhole is observed to be small [14, 44], allowing us to employ relatively large fully integrated cubic 64-node hexahedron elements with 3rd-order shape functions since the absence of element erosion prevents mass loss resulting in an artificial reduction of the capacity. Contact was taken care of by a penalty based node-to-surface algorithm. The effect of friction is disregarded in many studies, however, with ogival-ended projectiles frictional forces do exist. Zukas [45] recommended 0.01 to be used

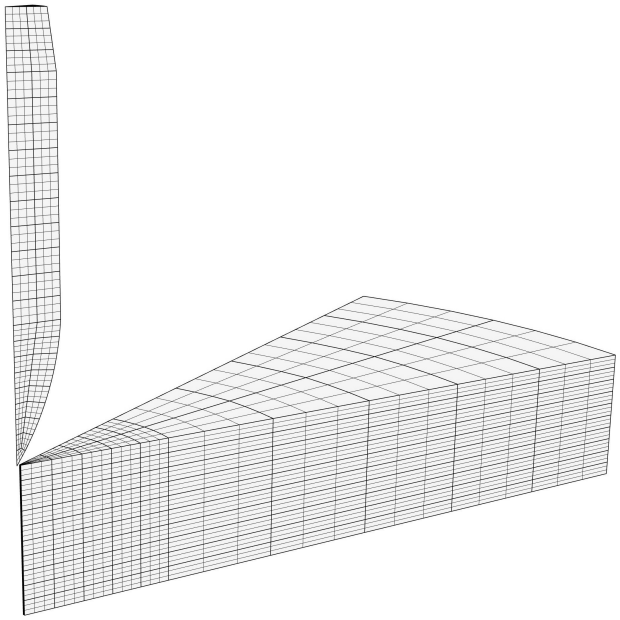

Figure 18: Solid element mesh used for the 10 mm thick profile in the IMPETUS Afea Solver. Two symmetry planes were assigned to enable modeling of only a 30° wedge.

as a dynamic friction coefficient. Ravid and Bodner [46] found that a friction coefficient of 0.1 is proposed in the literature for metal working applications, but they themselves advocated a value of 0.05 for impact situations. We realize that there might be frictional forces between the bullet and the plate, so in this study it was decided to use a frictional coefficient of 0.05 in the contact algorithm (see also [47]). However, it should be mentioned that including frictional effects in the sliding contact might contribute to non-conservative results [14, 43].

The AP-bullet was represented by its steel core with a rigid material formulation in all simulations, requiring only the density for steel, $\rho = 7850$ kg/m^3 as material input. Previous works have shown that the change in residual velocity is not significant if the entire AP-bullet with correct material input or only the core is used [6–9].

One finite element model was made with each of the material curves described by the parameters in Table 2. In other words, no attempt was made to describe the variation of the material parameters as a function of distance from the weld center line. NaMo does not provide material behavior from the center of the weld. Thus, in the simulations marked *weld* we have assumed the same behavior as at the location $x = 4.1$ mm from the weld center line.

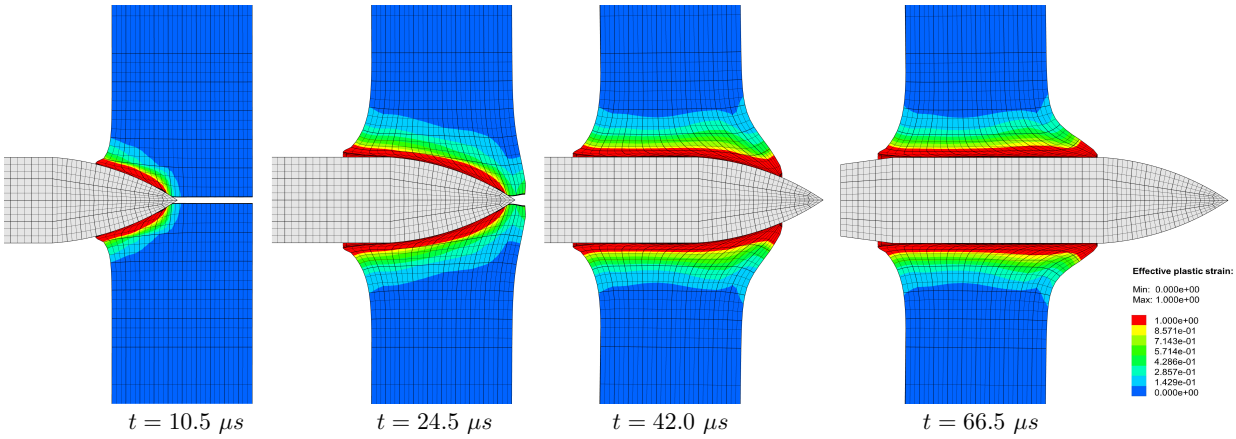

Figure 19: A typical perforation process displayed as a timelapse. The colors show accumulated plastic strain in the range $p \in [0; 1]$, and the mesh is reflected about the centerline to illustrate the pinhole (v_i = 450.0 m/s, v_r = 290.0 m/s).

5. Results and discussion

Fig. 19 shows the evolution of the equivalent plastic strain for a typical simulation of impact on the base material. Observe that no plastic strains accumulate outside a zone roughly one projectile radius (r = 3.05 mm) from the edge of the hole. This is consistent with the corresponding experiments. For impacts with lower velocities a zone of approximately one projectile diameter (d = 6.10 mm) is affected.

The numerical results are compared to the experimental results for the 10 mm thick profile in Fig. 20. For the base material, Fig. 20a, the ballistic limit velocity found numerically (v_{bl} = 344 m/s) is almost identical to the ballistic limit velocity found experimentally (v_{bl} = 347 m/s). Such a match is in many

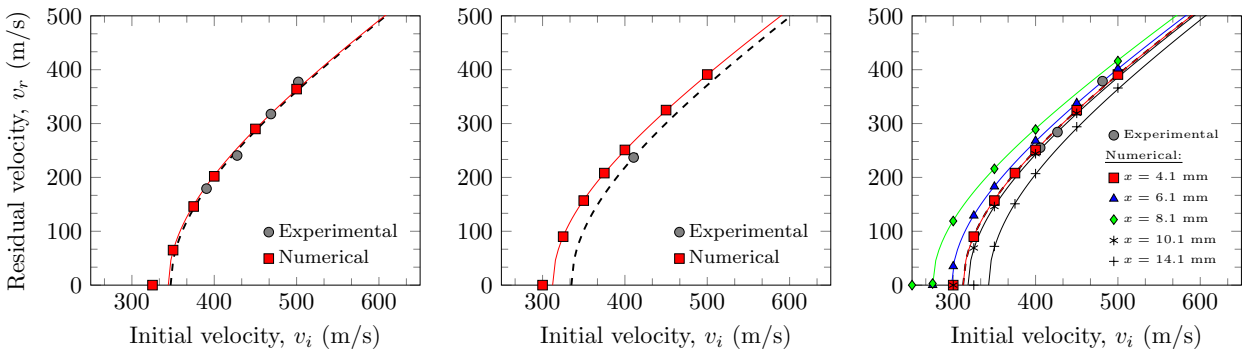

(a) Base material (b) Weld center line (c) HAZ

Figure 20: Experimental ballistic curves from (a) the base material, (b) the center of the welding zone, and (c) the HAZ; compared to purely numerical simulations.

ways coincidental seeing that many uncertainties exist in the experimental results and that a number of assumptions have been applied in the numerical model. In any case, the agreement between the experimental results and the numerical predictions is excellent.

Fig. 20b shows the results from the weld center line. Only one shot was fired directly at the weld-seam in the 10 mm thick profile. Furthermore, the constitutive behavior of the weld used in IMPETUS Afea Solver is presumed to be equal to the behavior of the material at a location 4.1 mm from the center of the weld. This seems to be a rational assumption based on the results from the hardness tests in Fig. 16. Here the numerically obtained ballistic limit velocity (v_{bl} = 312 m/s) underestimates the ballistic limit velocity (v_{bl} = 335 m/s) found from experiments with 6.9%. A lower ballistic limit velocity is a conservative result which is preferential from a design point of view.

Comparing results obtained from the HAZ, as seen in Fig. 20c, is more involved. In this area, only one ballistic limit velocity is available from the experiments, but several ballistic limit velocities have been found numerically since NaMo provided input to the constitutive model from multiple points at various distances x from the weld center line. The 7.62 mm AP-bullet has a finite diameter, so each impact will encompass several of the zones corresponding to the material behavior predicted by NaMo. By inspecting Fig. 20c we see that the experimentally obtained ballistic limit curve is surrounded by the curves obtained from simulations. The curves with the lowest and highest ballistic limit velocities are extracted 8.1 mm and 14.1 mm from the weld center line respectively, which is also suggested in Fig. 15. These points represent the lower and upper bound for the results from the HAZ. The v_{bl} for the experiment is 312 m/s, while the average between all the numerical values gives v_{bl} = 309.0 m/s, i.e. only 1.0% lower. To employ an average value for the numerical results is a crude way of simulating that the bullet hits several zones in the HAZ at the same time. Nevertheless, it illustrates the accuracy of the solution method. Another way of incorporating the zones would be to extract the spatially varying material parameters from NaMo and use this to assign the correct behavior to each integration point in the IMPETUS Afea Solver. That is left for further work.

Fig. 21 shows the bullet's residual velocity as a function of mesh density. Two cubic elements over the thickness yields no perforation. A softer response is achieved with an increasing mesh density, but no change in residual velocity can be seen if the number of elements over the thickness is increased above 10 elements. A typical analysis took approximately 3 min to run with 10 cubic elements over the thickness, but with 30 cubic elements over the target thickness the analysis time increased to over 60 min.

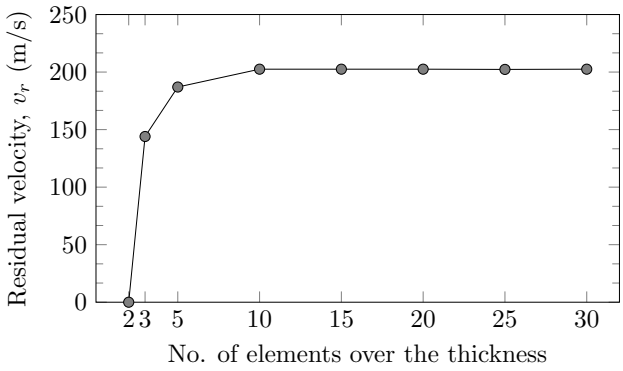

Figure 21: Results from the mesh-sensitivity study with initial velocity v_i = 400 m/s, and pinhole radius r = 0.25 mm.

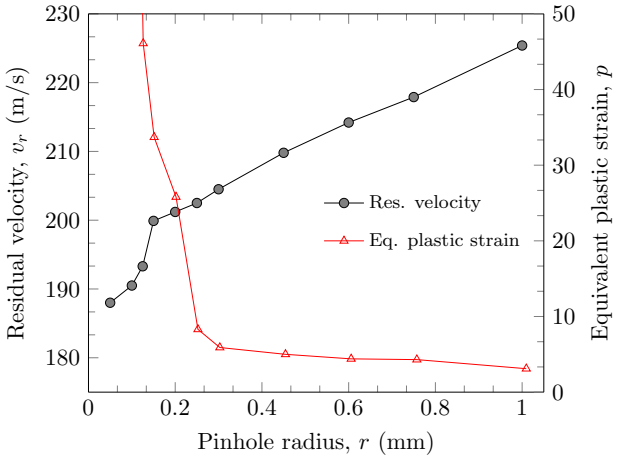

Figure 22: Results from the pinhole study with initial velocity v_i = 400 m/s, and 10 elemets over the thickness.

By replacing a fracture criterion with a pinhole we presume that only ductile hole-growth takes place. This is, with the exception of some rear-face petaling, true for the tests performed in this study. If more brittle failure mechanisms like rear-face spalling or fragmentation take place, a fracture criterion must be implemented to describe the more complex failure mode. However, for relatively thick profiles the rear-face petaling observed in this paper is generally not considered as a major energy dissipating mechanism [19], and a pinhole can safely be adopted.

The effect of the size of the pinhole is shown in Fig. 22. It is evident that for the conditions investigated in this study the radius of the pinhole affects the results. A linear decrease in residual velocity from 225.4 m/s to 201.2 m/s (i.e. 11%) is seen when reducing the pinhole radius from 1 mm to 0.20 mm. Below a 0.20 mm pinhole radius the maximum equivalent plastic strain in the analysis goes towards infinity because of unphysical element deformation. This is a numerical effect, and we conclude that the analyses cease to be valid below this pinhole size. Comparing these results to results seen in the literature (e.g. Camacho and Ortiz [44], Chen [48]) indicates that significantly smaller pinholes than those used here can be applied in 2D axisymmetric simulations and in simulations where friction is omitted.

6. Conclusions

In the experimental part of this paper, MIG-welded 10 mm, 20 mm and 30 mm thick AA6082-T6 aluminum extruded profiles were impacted by small-arms bullets to determine the effect of the heat affected zone (HAZ) on their ballistic limit velocity. In the tests, 7.62 mm AP-bullets were fired at the base material, weld metal and the HAZ with varying initial velocities. In all tests, the predominant failure mode was ductile-hole growth. The ballistic limit velocities were calculated with the Recht-Ipson equation for rigid sharp projectiles. We found a linear relationship between ballistic limit velocity and extrusion thickness for the respective targets. For all profiles the base material exhibited the highest ballistic limit velocity while the HAZ exhibited the lowest. The reduction of capacity was highest for the 10 mm thick profile where a 10% decrease in the ballistic limit velocity in the HAZ was observed.

The material test program included tension tests of the base material, and hardness tests through the weld (and in the base material). The 10 mm thick profile was found to behave similarly for the 0° and 90°-directions in terms of yield strength, flow stress and failure strain. For the 30 mm thick profile the yield strength for the 90°-direction was approximately 25 MPa lower than for the 0°-direction. A strength difference of almost 50 MPa was identified between the 10 and 30 mm profiles, where the 10 mm profile

was the strongest. Based on hardness measurements, the 20 mm profile was assumed to be similar to the 10 mm profile.

No experimental data was used in the numerical part of the paper. Here, the simulated temperature evolution during welding, the chemical composition and the artificial aging history were used to calculate the spatial distribution of the flow stress and subsequently the ballistic limit curves for the 10 mm thick profile. The thermal finite element model WELDSIM estimated accurately the temperature evolution during welding. A nanostructure model (NaMo) then calculated the flow stress curves that were used as input the in the IMPETUS Afea Solver. The final results, provided as ballistic limit velocities, are in very good agreement with the experimental results, especially if we consider that no experimental data whatsoever was used to calibrate the models. The trends from the simulations reflect the trends seen in the experiments, and the deviation is never more than 10%.

This paper shows that we can predict the ballistic behavior of AA6xxx aluminum alloys subjected to complex thermal histories without carrying out a single experiment. The fact that the numerical method described here gives results within 10% of the corresponding experiments suggests that this method can be very useful in the early design phase.

Acknowledgements

The financial support for this work from the Structural Impact Laboratory (SIMLab), Centre for Research-based Innovation (CRI) at the Norwegian University of Science and Technology, is gratefully acknowledged. The authors would like to thank Dr. Ida Westermann at SINTEF Materials and Chemistry for carrying out the hardness measurements, Mr. Trond Auestad for managing the ballistic tests, and Mr. Steffen Breivik and Mr. Espen Frøyen for their significant contribution in both experimental work and graphical design. The authors would also like to thank Mr. Steinar Lundberg at Hydal Aluminium Profiler AS as well as Mr. Nils Jakob Tjøstheim at Hydro Aluminium for planning and managing the welding process and the temperature measurements, respectively.

References

[1] Zukas JA, Scheffler DR. Impact effects in multilayered plates. International Journal of Solids and Structures 2001;38:3321–8.

[2] Børvik T, Hopperstad OS, Berstad T, Langseth M. Numerical simulation of plugging failure in ballistic penetration. International Journal of Solids and Structures 2001;38:6241–64.

[3] Dey S, Børvik T, Teng X, Wierzbicki T, Hopperstad OS. On the ballistic resistance of double-layered steel plates: An experimental and numerical investigation. International Journal of Solids and Structures 2007;44:6701–23.

[4] Rusinek A, Rodriguez-Martinez JA, Arias A, Klepaczko JR, Lopez-Puente J. Influence of conical projectile diameter on perpendicular impact of thin steel plate. Engineering Fracture Mechanics 2008;75:2946–3967.

[5] Iqbal MA, Gupta NK. Ballistic Limit of Single and Layered Aluminium Plates. Strain 2011;47:205–19.

[6] Børvik T, Dey S, Clausen AH. Perforation resistance of five different high-strength steel plates subjected to small-arms projectiles. International Journal of Impact Engineering 2009;36:948–64.

[7] Børvik T, Forrestal MJ, Warren TL. Perforation of 5083-H116 aluminium armor plates with ogive nose rods and 7.62 mm APM2 bullets. Experimental Mechanics 2010;50:969–78.

[8] Forrestal MJ, Børvik T, Warren TL. Perforation of 7075-T651 aluminium armor plates with ogive nose rods and 7.62 mm APM2 bullets. Experimental Mechanics 2010;50:1245–51.

[9] Holmen JK, Johnsen J, Jupp S, Hopperstad OS, Børvik T. Effects of heat treatment on the ballistic properties of AA6070 aluminium alloy. International Journal of Impact Engineering 2013;57:119–33.

[10] Deschamps Y, Brechet Y. Influence of predeformation and ageing of an Al-Zn-Mg alloy-II. Modeling of precipitation kinetics and yield stress. Acta Materialia 1999;47:293–305.

[11] Myhr OR, Grong Ø, Andersen SJ. Modelling of the age hardening behaviour of Al-Mg-Si alloys. Acta Materialia 2001;49:65–75.

[12] Myhr OR, Grong Ø, Pedersen KP. A Combined Precipitation, Yield Strength, and Work Hardening Model for Ag-Mg-Si Alloys. Metallurgical and Materials Transactions 2010;41A:2276–89.

[13] Myhr OR, Grong Ø. Modeling of Metallurgical Microstructure Evolution in Fusion Welding. ASM Handbook 2011;41A:797–818.

[14] Johnsen J, Holmen JK, Myhr OR, Hopperstad OS, Børvik T. A nano-scale material model applied in finite element analysis of aluminium plates under impact loading. Computational Materials Science 2013;79:724–35.

[15] Kamp N, Sullivan A, Tomasi R, Robson JD. Modelling of heterogeneous precipitate distribution evolution during friction stir welding process. Acta Materialia 2006;54:2003–14.

[16] Kamp N, Sullivan A, Robson JD. Modelling of friction stir welding of 7xxx aluminium alloys. Materials Science and Engineering A 2007;466:246–55.

[17] Grujicic M, Arakere A, Yen C, Cheeseman BA. Computational Investigation of Hardness Evolution During Friction-Stir Welding of AA5083 and AA2139 Aluminum Alloys. Journal of Materials Engineering and Performance 2011;20:1097–108.

[18] Grujicic M, Arakere A, Pandurangan B, Hariharan A, Yen C, Cheeseman BA. Development of a Robust and Cost-Effective Friction Stir Welding Process for Use in Advanced Military Vehicles. Journal of Materials Engineering and Performance 2011;20:11–23.

[19] Grujicic M, Pandurangan B, Arakere A, Yen C, Cheeseman BA. Friction Stir Weld Failure Mechanisms in Aluminum-Armor Structures Under Ballistic Impact Loading Conditions. Journal of Materials Engineering and Performance 2014;22:30–40.

[20] Grujicic M, Snipes JS, Galgalikar R, Ramaswami S, Yavari R, Yen C, et al. Ballistic-Failure Mechanisms in Gas Metal Arch Welds of Mil A46100 Armor-Grade Steel: A Computational Investigation. Journal of Materials Engineering and Performance 2014;23:3108–25.

[21] Sullivan A, Derry C, Robson JD, Horsfall I, Prangnell PB. Microstructure simulation and ballistic behaviour of weld zones

in friction stir welds in high strength aluminium 7xxx plate. Materials Science and Engineering A 2011;528:3409–22.

[22] Fjær HG, Myhr OR, Klokkehaug S, Holm S. Advances in aluminum weld simulations applying WeldSim. Proceedings of the 11th International Conference on Computer Technology in Welding, NIST Special Publication 973 2001;:251–63, (Eds.) T.A. Siewert and C. Pollock, (Washington).

[23] Myhr OR, Klokkehaug S, Grong Ø, Fjær HG, Kluken AO. Modelling of Microstructure Evolution, Residual Stresses and Distortions in 6082-T6 Aluminum Weldsments. Welding Journal 1998;77:286–92.

[24] IMPETUS Afea AS . IMPETUS Afea Solver; Cited 2014-20-10. http://www.impetus-afea.com.

[25] CEN . EN 1090-3. Execution of steel structures and aluminium structures Part 3: Technical requirements for aluminium structures; 2008. European Committee for Standardization.

[26] Safra SPA . Safra SPA; Cited 2014-10-20. http://www.safraspa.it.

[27] Fourmeau M, Børvik T, Benallal A, Lademo OG, Hopperstad OS. On the plastic anisotropy of an aluminium alloy and its influence on constrained multiaxial flow. International Journal of Plasticity 2011;27:2005–25.

[28] Myhr OR, Grong Ø, Fjær HG, Marioara CD. Modelling of the microstructure and strength evolution in Al-Mg-Si alloys during multistage thermal processing. Acta Materialia 2004;52:4997–5008.

[29] Breivik SMW, Thomsen EF. Perforation of Welded Aluminium Structures. Master's thesis; SIMLab - Norwegian University of Science and Technology, NTNU; 2014.

[30] Børvik T, Langseth M, Hopperstad OS, Malo KA. Ballistic penetration of steel plates. International Journal of Impact Engineering 1999;22:855–86.

[31] Børvik T, Hopperstad OS, Langseth M, Malo KA. Effect of target thickness in blunt projectile penetration of Weldox 460 E steel plates. International Journal of Impact Engineering 2003;28:413–64.

[32] Recht RF, Ipson TW. Ballistic perforation dynamics. Journal of Applied Mechanics 1963;30:384–90.

[33] Rosenberg Z, Dekel E. On the deep penetration and plate perforation by rigid projectiles. International Journal of Solids and Structures 2009;45:4169–80.

[34] Fjær HG, Liu J, M'Hamdi M, Lindholm D. On the Use of Residual Stresses from Welding Simulations in Failure Assessment Analyses for Steel Structures; chap. Mathematical Modelling of Weld Phenomena 8. Verlag der Techn. Univ. Graz; 2007, p. 998–1011.

[35] Fjær HG, Bjørneklett BI, Myhr OR. Microstructure based modelling of Al-Mg-Si alloys in Development of Local Heating Processes for Automotive Structures. Trends in Materials and Manufacturing Technology for Transportation Industry and Powder Metallurgy Reseach and Development in the Transportation Industry, Warrendale, PA, USA 2005;.

[36] Fjær HG, Aune R, M'Hamdi M. Modelling the development of stresses during single and multipass welding of a ferritic steel in an instrumented restraint cracking test. Modelling of Casting, Welding, and Advanced Solidification Processes- XII, TMS, USA 2009;:571–8.

[37] Myhr OR, Grong Ø, Klokkehaug S, Fjær HG. Modelling of the microstructure and strength evolution during ageing and welding of Al-Mg-Si alloys; chap. Mathematical Modelling of Weld Phenomena 6 (Editor: H. Cerjak). The institute of Materials; 2002, p. 337–63.

[38] Dørum C, Lademo OG, Myhr OR, Berstad T, Hopperstad OS. Finite element analysis of plastic failure in heat-affected zone of welded aluminium connections. Computers & Structures 2010;88:519–28.

[39] Myhr OR, Grong Ø. Novel Modelling Approach to Optimisation of Welding Conditions and Heat Treatment Schedules for

Age Hardening Al Alloys. Science and Technology of Welding and Joining 2009;14:621–32.

[40] Bridgman PW. The stress distribution at the neck of a tensile specimen. Transactions of the American Society for Metals 1944;32:553–72.

[41] Børvik T, Hopperstad OS, Berstad T, Langseth M. A computational model of viscoplasticity and ductile damage for impact and penetration. European Journal of Mechanics A/Solids 2001;20:685–712.

[42] Chen Y, Clausen AH, Hopperstad OS, Langseth M. Stress-strain behaviour of aluminium alloys at a wide range of strain rates. International Journal of Solids and Structures 2009;46:3825–35.

[43] Børvik T, Olovsson L, Dey S, Langseth M. Normal and oblique impact of small arms bullets on AA6082-T4 aluminium protective plates. International Journal of Impact Engineering 2011;38:577–89.

[44] Camacho GT, Ortiz M. Adaptive Lagrangian modelling of ballistic penetration of metallic targets. Computer Methods in Applied Mechanics and Engineering 1997;142:269–301.

[45] Zukas JA. High Velocity Impact Dynamics. 1st ed.; John Wiley & Sons, Inc.; 1990.

[46] Ravid M, Bodner SR. Dynamic perforation of viscoplastic plates by rigid projectiles. International Journal of Engineering Sciences 1983;21:577–91.

[47] Børvik T, Hopperstad OS, Berstad T, Langseth M. Perforation of 12 mm thick steel plates by 20 mm diameter projectiles with blunt, hemispherical and conical noses, part II: Numerical simulations. International Journal of Impact Engineering 2002;27:37–64.

[48] Chen EP. Finite element simulation of perforation and penetration of aluminum targets by conical-nosed steel rods. Mechanics of Materials 1990;:107–15.